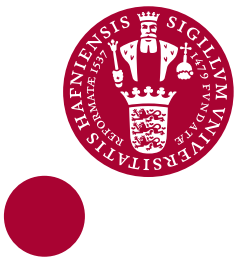

Visibility simulation of realistic grating interferometers including grating geometries and energy spectra

Harti, Ralph P.; Kottler, Christian; Valsecchi, Jacopo; Jefimovs, Konstantins; Kagias, Matias; Strobl, Markus; Grunzweig, Christian

Published in:
Optics Express

DOI:
10.1364/OE.25.001019

Publication date:
2017

Document version
Publisher's PDF, also known as Version of record

Research Article | Vol. 25, No. 2 | 23 Jan 2017 | OPTICS EXPRESS 1019

Optics EXPRESS

Visibility simulation of realistic grating interferometers including grating geometries and energy spectra

RALPH P. HARTI,[1,2,*] CHRISTIAN KOTTLER,[3] JACOPO VALSECCHI,[1,2] KONSTANTINS JEFIMOVS,[1,4] MATIAS KAGIAS,[1,4] MARKUS STROBL,[5,6] AND CHRISTIAN GRÜNZWEIG[1]

[1] *Paul Scherrer Institut, 5232 Villigen-PSI, Switzerland*
[2] *University of Geneva, 1211 Geneva, Switzerland*
[3] *Federal Institute of Metrology, 3003 Berne-Wabern, Switzerland*
[4] *ETH Zurich, 8092 Zurich, Switzerland*
[5] *European Spallation Source E.R.I.C., 22100 Lund, Sweden*
[6] *Niels Bohr Institute, 2100 Copenhagen, Denmark*
[*] *Ralph.Harti@psi.ch*

Abstract: The performance of X-ray and neutron grating interferometers is characterised by their visibility, which is a measure for the maximum achievable contrast. In this study we show how the real grating geometry in a grating interferometer with three gratings impacts the interference and self projection that leads to visibility in the first place. We quantify the individual contributions of wavelength distributions and grating shapes in terms of visibility reduction by determining the absolute as well as relative effect of each contribution. The understanding of the impact of changed geometry and wavelength distributions on the interference of neutrons/X-rays allows us to present the first fully quantitative model of a grating interferometer setup. We demonstrate the capability of the simulation framework by building a model of the neutron grating interferometer at the ICON beamline and directly comparing simulated and measured visibility values. The general nature of the model makes it possible to extend it to any given grating interferometer for both X-rays and neutrons.

OCIS codes: (050.1950) Diffraction gratings; (100.3175) Interferometric imaging; (070.7345) Wave propagation.

References and links

1. M. Strobl, B. Betz, R. P. Harti, A. Hilger, N. Kardjilov, I. Manke, and C. Grünzweig, "Wavelength-dispersive dark-field contrast: micrometre structure resolution in neutron imaging with gratings," J. Appl. Crystallogr. **49**(2), 569–573 (2016).
2. F. Pfeiffer, T. Weitkamp, O. Bunk, and C. David, "Phase retrieval and differential phase-contrast imaging with low-brilliance X-ray sources," Nature Phys. **2**(4), 258–261 (2006).
3. F. Pfeiffer, M. Bech, O. Bunk, P. Kraft, E. F. Eikenberry, Ch. Brönnimann, C. Grünzweig, and C. David, "Hard-X-ray dark-field imaging using a grating interferometer," Nat. Mater. **7**(2), 134–137 (2008).
4. F. Pfeiffer, C. Grünzweig, O. Bunk, G. Frei, E. Lehmann, and C. David, "Neutron phase imaging and tomography," Phys. Rev. Lett. **96**(21), 215505 (2006).
5. C. Grünzweig, C. David, O. Bunk, M. Dierolf, G. Frei, G. Kühne, J. Kohlbrecher, R. Schäfer, P. Lejcek, H. M. R. Rønnow, and F. Pfeiffer, "Neutron decoherence imaging for visualizing bulk magnetic domain structures," Phys. Rev. Lett. **101**(2), 025504 (2008).
6. M. Strobl, C. Grünzweig, A. Hilger, I. Manke, N. Kardjilov, C. David, and F. Pfeiffer, "Neutron dark-field tomography," Phys. Rev. Lett. **101**(12), 123902 (2008).
7. B. Betz, P. Rauscher, R. P. Harti, R. Schäfer, H. Van Swygenhoven, A. Kaestner, J. Hovind, E. Lehmann, and C. Grünzweig, "In-situ visualization of stress-dependent bulk magnetic domain formation by neutron grating interferometry," Appl. Phys. Lett. **108**(1), 012405 (2016).
8. P. Willendrup, E. Farhi, and K. Lefmann, "McStas 1.7 - a new version of the flexible Monte Carlo neutron scattering package," Physica B **350**(1), E735–E737 (2004).
9. K. Lefmann, P. K. Willendrup, L. Udby, B. Lebech, K. Mortensen, J. O. Birk, K. Klenø, E. Knudsen, P. Christiansen, J. Saroun, J. Kulda, U. Filges, M. Konnecke, P. Tregenna-Piggott, J. Peters, K. Lieutenant, G. Zsigmond, P. Bentley, and E. Farhi, "Virtual experiments: the ultimate aim of neutron ray-tracing simulations," J. Neutron Res. **16**(3), 97–111 (2008).

#279654 http://dx.doi.org/10.1364/OE.25.001019
Journal © 2017 Received 2 Nov 2016; revised 23 Dec 2016; accepted 25 Dec 2016; published 12 Jan 2017

Optics EXPRESS

10. W. Greiner, *Quantum mechanics: An introduction* (Springer Science & Buisness Media, 2000).
11. H. Rauch and S. Werner, *Neutron interferometry*, (Oxford University, 2015), 2nd ed.
12. M. Engelhardt, C. Kottler, O. Bunk, C. David, C. Schroer, J. Baumann, M. Schuster, and F. Pfeiffer, "The fractional Talbot effect in differential x-ray phase-contrast imaging for extended and polychromatic x-ray sources," J. Microsc. **232**(1), 145–157 (2008).
13. T. Weitkamp and C. David, "Tomography with grating interferometers at low-brilliance sources," Proc. SPIE **6318**, 63180S (2006).
14. S. Hipp, M. Willner, J. Herzen, S. D. Auweter, M. Chabior, J. Meiser, K. Achterhold, J. Mohr, and F. Pfeiffer, "Energy-resolved visibility analysis of grating interferometers operated at polychromatic X-ray sources," Opt. Express **22**(25), 30394–30409 (2014).
15. S. Peter, P. Modregger, M. K. Fix, W. Volken, D. Frei, P. Manser, and M. Stampanoni, "Combining Monte Carlo methods with coherent wave optics for the simulation of phase-sensitive X-ray imaging," J. Synchrotron Radiat. **21**(3), 613–622 (2014).
16. T. Weber, P. Bartl, F. Bayer, J. Durst, W. Haas, T. Michel, A. Ritter, and G. Anton, "Noise in x-ray grating-based phase-contrast imaging," Med. Phys. **38**(7), 4133–4140 (2011).
17. P. Bartl, F. Bayer, J. Durst, W. Haas, T. Michel, A. Ritter, T. Weber, and G. Anton, "Grating-based high energy X-ray interferometry with the Medipix-detector in simulation and measurement," J. Instrum. **5**(10) P10008 (2010).
18. W. Haas, P. Bartl, F. Bayer, J. Durst, T. Grund, J. Kenntner, T. Michel, A. Ritter, T. Weber, G. Anton, and J. Hornegger, "Performance analysis of X-Ray phase-contrast interferometers with respect to grating layouts," in Proceedings of the IEEE Nuclear Science Symposuim & Medical Imaging Conference (2010), pp. 3176–3178.
19. A. P. Kaestner, S. Hartmann, G. Kühne, G. Frei, C. Grünzweig, L. Josic, F. Schmid, and E. H. Lehmann, "The ICON beamline - A facility for cold neutron imaging at SINQ," Nucl. Instr. Meth. Phys. Res. A **659**(1), 387–393 (2011).
20. C. Grünzweig, F. Pfeiffer, O. Bunk, T. Donath, G. Kühne, G. Frei, M. Dierolf, and C. David, "Design, fabrication, and characterization of diffraction gratings for neutron phase contrast imaging," Rev. Sci. Instrum. **79**(5), 1–6 (2008).
21. M. Morgano, S. Peetermans, E. H. Lehmann, T. Panzner, and U. Filges, "Neutron imaging options at the BOA beamline at Paul Scherrer Institut," Nucl. Instr. Meth. Phys. Res. A **754**(5), 46-56 (2014).
22. T. Thüring, M. Abis, Z. Wang, C. David, and M. Stampanoni, "X-ray phase-contrast imaging at 100 keV on a conventional source," Sci. Rep. **4** 5198 (2014).

1. Introduction

The multimodal imaging technique grating interferometry is an increasingly popular method for both X-rays and neutrons. It provides images based on the wavelike nature of the particle beam used to conduct the measurement. For X-ray grating interferometry (xGI) the particles are photons and in case of neutron grating interferometry (nGI) neutrons are used to generate images. In any case grating interferometry provides three images with different information content. One is the transmission image (TI), which holds information on attenuation. The second one is the differential phase contrast image (DPCI). It images the phase shift gradient which acts on the particle wave while passing through the sample. The third signal is the so called dark-field image (DFI), which results from the scattering properties of the sample for very small angles [1]. The feasability as well as numerous applications have been presented, both with X-rays [2, 3] and with neutrons [4–7].

Any of the resulting signals are a consequence of interference of the incoming beam, after traversing a phase grating. The periodic structure of the diffraction grating creates an interference pattern which projects the structure of the grating at the so called Talbot distance. These effects are a direct result of interference. This means that to understand the behaviour of grating interferometers the beam has to be treated as a wave no matter if the beam is made of photons or massive particles, such as neutrons, which are often simulated as particles [8, 9]. The particle wave duality has been proposed a long time ago [10] and manifests itself in the deBroglie equation that assigns a wavelength to massive particles. Thus neutrons can be considered a wave and wave optical descriptions of interference effects can be used to understand the nGI [11] as well as the xGI.

Previous work on simulating grating interferometers was driven by its application for synchrotrons and X-ray tube sources. The key feature that most work was concerned with is the spectral distribution of the X-ray tube source and its impact on the performance of the grating interferometer [12–14] or even the actual simulation of images [15]. Tube sources emit a large

Optics EXPRESS

range of energies and the understanding of the impact of spectral distributions on the visibility is often driven by increasing the setup performance and thus lowering the dose for patients in medical applications. However no study included the real geometry of the gratings and it was thus not possible to simulate the absolute value of the visibility for a specific setup [16, 17]. The microfabrication process for the gratings leaves imperfect grating geometries, which is most important when it comes to gratings with fairly small pitches, such as the G2 grating in nGIs, which has a typical period of around 4 µm.

We present a simulation framework that includes, besides the spectral distribution of the incoming beam, the real geometry of the gratings used in a grating interferometer. Unlike Haas et al. [18] we also consider the imperfect height distribution and trench shape of the gratings and are thus able to get results that are directly comparable to measured values without the need to fit any initial values, thus indicating a physically feasible model of the setup. We present the first simulation of a neutron grating interferometer by building a model of the nGI at the ICON beamline at the Paul Scherrer Institut (PSI) to show the potential of the simulation framework. Furthermore we compare different imaging procedures, as well as sets of gratings and use the fully quantitative model to extract the individual contributions that are responsible for the performance of the nGI at ICON.

2. Experimental setup and simulation parameters

The experiments presented in this work were conducted at the Swiss Spallation Neutron Source (SINQ) at the Paul-Scherrer-Institut (PSI) using the ICON [19] facility for imaging with cold neutrons. It consists of three gratings G0, G1 and G2, as indicated in the inlet of Fig. 1a. The absorption grating G0 is made of gadolinium (Gd) and acts as a source grating by introducing the required spatial coherence to the beam. The second grating (G1) is a so called phase grating made of silicon (Si) and is designed such that it introduces a periodic π-phase modulation to the beam and thus creates the interference patterns required for grating interferometer measurements. The desired phase shift (Φ) is defined by the structure height of the grating, which is described by

$$\Phi = n_{SLD} \cdot \lambda \cdot h, \tag{1}$$

with the neutron scattering length density of the material n_{SLD} the wavelength λ and the height of the structure h.

The third grating (G2) is another absorption grating made of gadolinium, which represents the period of the self-projection of G1 as a consequence of the Talbot effect. This grating is needed because the period of the self projection is below the detector resolution and by introducing a G2 grating a spatial stepping of one grating can be used to transfer the self projection into an intensity oscillation in each pixel of the detector. The ideal grating parameters are determined using the equations in [20] leading to a set of gratings with following specifications:

- **G0:** Period $p_0 = 1076\mu m$, duty cycle $DC = 0.4$, material Gd, height $20\mu m$
- **G1:** Period $p_1 = 7.97\mu m$, duty cycle $DC = 0.5$, material Si, height $37\mu m$
- **G2:** Period $p_1 = 4\mu m$, duty cycle $DC = 0.5$, material Gd, height $8\mu m$

and a distance of 5.23 m between G0 and G1 and 19.4 mm between G1 and G2.

The neutrons were detected using a standard $^6LiF/ZnS$ scintillator with a thickness of 200 µm coupled to an Andor Neo sCMOS camera with 2160 x 2560 pixels and a pixel size of 6.5 µm. In order to retrieve the visibility values we stepped the G0 grating in 17 steps over one period with an exposure time of 30s per step and recorded the images with a 4x4 binning. In order to compensate for detector noise we applied a dark-current correction.

Optics EXPRESS

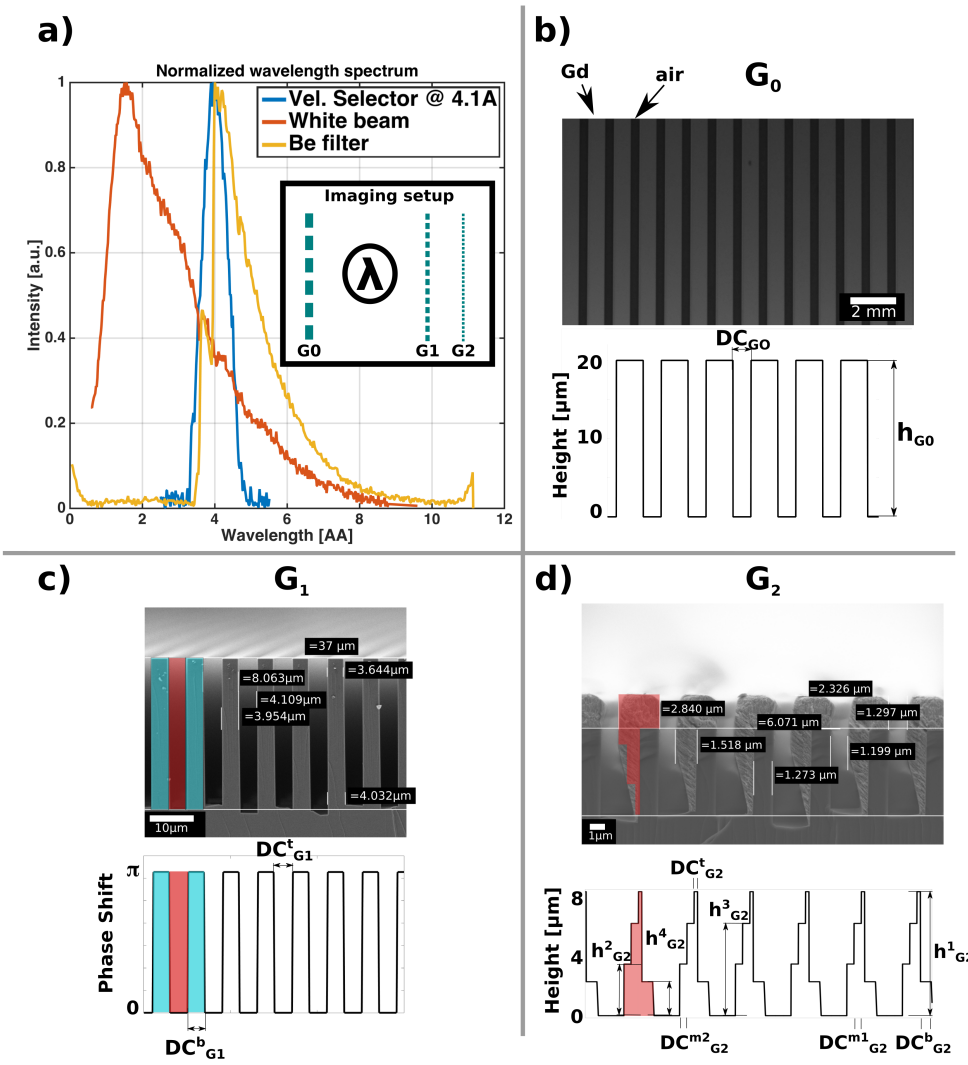

Fig. 1. Grating geometries and spectral distributions for neutron grating interferometry. a) Examples of neutron energy distributions considered in the presented work. The inlet shows the setup with the three gratings (G0, G1, G2) and the position of the wavelength selecting device between G0 and G1, indicated with λ. b) Optical image of the G0 grating (top view) made of gadolinium (Gd). The arrows indicate gadolinium trenches (Gd) and the gaps between them (air). The plot below the image shows how its properties are considered in the presented simulation. c), d) Scanning electron microscopy images of G1 and G2 and the according representation in the simulation, including the parameters needed to define the structures.

The model we developed in this work takes a variety of different aspects of real grating interferometers into account to describe the real geometry of the fabricated gratings as close as possible. Fig. 1 shows an overview of the experimental setup, as well as the multitude of input parameters that is given to the simulation. Fig. 1a depicts a schematic representation of the three grating setup, including G0, G1 and G2. In our setup we place the velocity selector, indicated by λ, between G0 and G1. Fig. 1a also shows three normalised neutron wavelength spectra used

Optics EXPRESS

during the simulations and measurements:

- **White beam:** Full ICON spectrum
- **Be-filter:** Beryllium filtered ICON spectrum, cut-off ≥ 4Å
- **Velocity selector:** Monochromatic beam with $\frac{\Delta\lambda}{\lambda} = 15\%$.

These are a representative subset of the spectra being used for both simulation and experiment. Fig. 1b shows an optical image of the G0 grating, Fig. 1c a scanning electron microscopy (SEM) image of G1 and Fig. 1d an SEM image of G2. It can be seen directly, that the real geometries deviate from the ideally proposed grating parameters. In the following section we will show how the grating properties as well as their real geometry are defined in our simulation.

Defining G0

G0 is an absorption grating made of gadolinium (Gd), for highest possible neutron absorption. The absorption properties are calculated from the thickness of the Gd layers with

$$T(\lambda) = \frac{1}{e^{\frac{d}{a_l}}}. \tag{2}$$

The wavelength (λ) dependent transmission is a consequence of the thickness (d) and the attenuation length (a_l), which is defined as $\frac{\lambda_d}{\lambda} \cdot a_{ld}$ with a_{ld} being the penetration depth of Gd at a neutron wavelength of 4.1Å ($a_{ld} = 2.92\,\mu m$). The absorption is defined relative to the design wavelength (λ_d) of the setup, which allows us to incorporate the strongly wavelength dependent neutron absorption over the whole spectrum used to record images.

The geometry of G0 is assumed to be perfect, because the large period of the grating makes it possible to use laser ablation with high precision for manufacturing. Thus the parameters that describe the G0 geometry as indicated in Fig. 1b are $h_{G0} = 20\,\mu m$ and $DC_{G0} = 0.4$.

Defining G1

G1 is a phase grating that is used to introduce well defined phase shifts into the beam. The realistic geometry of G1 can be described by specifying the grating width on top and on the bottom and then interpolate between them. This truncated shape is chosen to represent the under-etching which is a classical artefact when it comes to the production of high aspect ratio structures using chemical wet etching [20]. As shown in Fig. 1c the top part of the trenches of the G1 are 3.644 µm wide and the bottom part 4.032 µm. In the simulation software we represented this as a step wise approximation of over 100 steps from the top of the structure (duty cycle 0.45) down to the bottom of the structure with the design duty cycle of 0.5.

We defined the grating with the relative phase shift (Φ) the neutrons get by passing through the structure. The desired π-shift at the design wavelength of 4.1Å is achieved at a height of 37 µm. In analogy to the absorption properties of G0 we defined the phase shift of G1 relative to the phase shift at the design wavelength:

$$\Phi_l = \frac{\lambda_d}{\lambda} \cdot \Phi_{ideal}. \tag{3}$$

Φ_{ideal} is the designed phase shift, λ_d the design wavelength and λ the evaluated wavelength. That way the G1 grating is defined by the energy dependent phase shift (Φ_l) it introduces on the incoming beam.

Despite the relatively small imperfections of G1 its impact on the emerging interference pattern is quite severe, as we show in Fig. 2. The top left shows the parameters used for the geometry variation and the top right indicates the values used for a perfect geometry representation and

Optics EXPRESS

a real geometry representation. One can see that the only difference is the duty cycle at the top of the structure (DC^t_{G1}) that varies slightly. However looking at the bottom of Fig. 2 it is clearly visible how this slight imperfection changes the Talbot carpet from the perfect to the real geometry. Especially the line scans present extra features that are not existent in the perfect geometry. We will later quantify the influence of this effect on the visibility.

Defining G2

The last grating is G2 with the relatively small period of 4 µm which makes its fabrication very challenging and thus leads to a quite imperfect shape, which we approximated with a four-step structure.

The bottom right of Fig. 1d shows both the real G2 structure and the model. The model is defined by four different heights (h^1_{G2} = 8.4 µm, h^2_{G2} = 3.5 µm, h^3_{G2} = 6.25 µm and h^4_{G2} = 2.3 µm), which represent the Gd height in the real structure reasonably well. Each height has a different duty cycle assigned: DC^t_{G2} = 0.94, DC^{m1}_{G2} = 0.89, DC^{m2}_{G2} = 0.89 and DC^b_{G2} = 0.78. A comparison of real and modelled structure height is indicated with the red area. The left part of each trench in the grating has a higher structure due to the fabrication process which deposits Gd sideways [20]. This behaviour is modelled with a step-wise approximation.

Defining spectral distribution

The last thing that is left to be described by the simulation framework is the realistic representation of the incoming neutron spectrum. We achieved this by using the real measured spectrum and spline interpolate between the measured points. While this is directly achievable for white beam and beryllium filtered spectra it is challenging to describe the effect of the velocity selector for varying wavelengths. We implemented the velocity selector via its relative behaviour to the spectrum at 4.1Å and shifted the spectrum to the desired wavelength while keeping the wavelength resolution of $\frac{\Delta\lambda}{\lambda}$ = 15% constant. This way we were able to extrapolate a measured spectrum at 4.1 Å to spectra at 3, 3.5, 4.5, 5 and 6 Å with the real behaviour of the velocity selector according to its specifications.

3. Simulation

The simulation results of the setup presented in this work are based on a well established wave-optics simulation approach that is commonly used in qualitatively simulating X-ray grating interferometers [12–15] and was adapted to simulate the nGI setup at ICON. Its fundamental idea is to define an incoming wave front at G1 ($D_{G1}(y)$) and propagate it using a free space propagator ($P_{real}(y, d, \lambda)$) based on Fresnel interference to the fractional Talbot distance. This can be written as a convolution of both:

$$D_{@dt}(y, d, \lambda) = D_{G1}(y) * P_{real}(y, d, \lambda). \tag{4}$$

The result is a wave function ($D_{@dt}(y, d, \lambda)$) at the fractional Talbot distance (d_t). The convolution in eq. 4 is done in Fourier space, thus applying the free-space propagator in Fourier space ($P(Y, d, \lambda)$) to the Fourier transform of $D_{G1}(y)$:

$$\mathcal{F}(D_{@dt}(y, d, \lambda)) = \mathcal{F}(D_{G1}(y)) \cdot P(Y, d, \lambda). \tag{5}$$

$P(Y, d, \lambda)$ is defined as:

$$P(Y, d, \lambda) = e^{-i\pi\lambda d Y^2}, \tag{6}$$

with λ being the wavelength, d the distance and y the spatial coordinate. Y is the representation of y in Fourier space. After this operation an inverse Fourier transform brings the wavefunction back to real space.

Optics EXPRESS

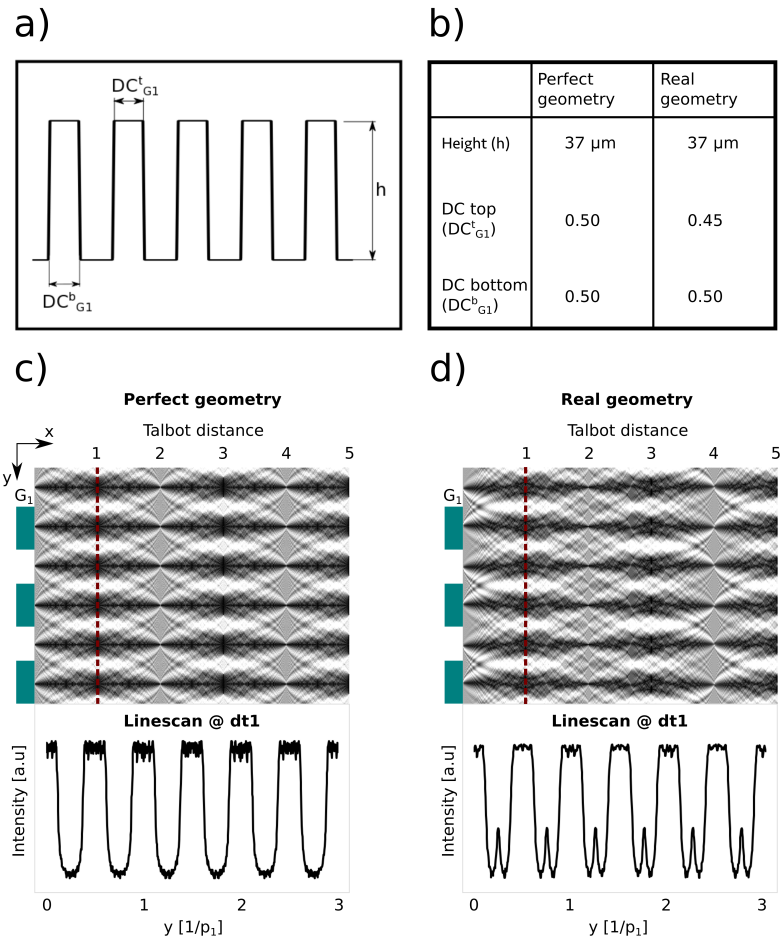

Fig. 2. The impact of slight imperfections in G1 on the Talbot carpet. a): Schematic of the geometrical parameters. b): Geometrical parameters for perfect and real geometry. c),d): Calculated Talbot carpets for both geometries up to the fifth fractional Talbot distance at 4.1 Å. The linescans show the intensity distribution at the first fractional Talbot distance and are plotted as a function of multiple of the G1 period (p_1).

For the evaluation of the visibility $D_{@dt}(y, d, \lambda)$ is convoluted with the absorption properties of the grating G2 ($G2(y)$)

$$D_{G2}^{eval}(y, d, \lambda) = D_{@dt}(y, d, \lambda) * G2(y), \tag{7}$$

resulting in $D_{G2}^{eval}(y, d, \lambda)$ which represents the intensity distribution at the detector in case of a perfectly uniform and parallel beam. In reality we use a G0 absorption grating to create an array of line sources. To simulate this effect we convolute $D_{G2}^{eval}(y, d, \lambda)$ with the projection of the absorption properties of G0 ($G0(y)$),

$$D^{eval}(y, d, \lambda) = D_{G2}^{eval}(y, d, \lambda) * G0(y), \tag{8}$$

to simulate the real intensity distribution at the detector ($D^{eval}(y, d, \lambda)$).

$D^{eval}(y, d, \lambda)$ can then be analysed to retrieve the visibility (contrast) of the grating setup. This is done by determining the amplitude of the sinusoidal shaped $D^{eval}(y, d, \lambda)$ function such

Optics EXPRESS

that the visibility (V) can be retrieved:

$$V(y,d,\lambda) = \frac{max(D^{eval}(y,d,\lambda)) - min(D^{eval}(y,d,\lambda))}{max(D^{eval}(y,d,\lambda)) + min(D^{eval}(y,d,\lambda))}. \quad (9)$$

The visibility is a direct indication for the performance of a grating interferometer and is usually highest at the design wavelength of the system. However a variety of different spectral distributions are possible, such as velocity selector, Be-filter or white beam. We can only create a fully quantitative model description of the nGI when the spectral distribution is considered together with geometrical imperfections due to the grating fabrication.

As one can see in eq. 6 $P(Y,d,\lambda)$ depends on the selected wavelength. In order to incorporate wavelength distributions we weight the wavelength according to the relative intensity in the spectrum. This way we can include any spectrum, such as white beam, or energy selected wavelength distributions. The desired wavelengths were experimentally selected with a turbine velocity selector between G0 and G1. The wavelength resolution of $\frac{\Delta\lambda}{\lambda} \sim 15\%$ is a good compromise between flux and energy resolution.

4. Results

The complete simulation model, including the grating geometry and the spectral distribution, can be used to directly simulate the performance of the nGI at ICON and compare the absolute values as well as the behaviour with varying setup parameters directly to experimentally determined visibilities. Fig. 3 shows the direct comparison of measurement and simulation. The error bars for the measured values are the standard deviation of extracted visibility within the field of view. The field of view from which the data were extracted in each measurement is indicated by the red box on the visibility map in the inlet of Fig.3. The whole grating area was used for the visibility extraction, leaving only area without gratings outside of the red box.

Visibility simulation for different measurement conditions

A total of nine comparisons between experiment and simulation have been performed, as can be seen in Fig. 3. The setup for the first eight comparisons has a design wavelength of 4.1 Å. The simulation validation for this configuration is indicated by the green box. As mentioned before the wavelength selection was accomplished with a velocity selector with a wavelength resolution of $\frac{\Delta\lambda}{\lambda} \sim 15\%$. For the other wavelength selections the velocity selector was set to the according wavelength. In terms of simulating the visibility for wavelength variations we kept the simulation model the same except for the varying spectrum that we shifted towards the desired wavelength while keeping the velocity selector performance constant. The comparison of experiments and simulation for the velocity selector measurements indicate that we can describe the wavelength behaviour of the visibility quantitatively and can also predict the visibility with high accuracy for wavelengths other than the design wavelength of the setup.

Grating interferometers are sometimes used with broader spectra, such as white beam or Be-filtered neutron beams. In order to check if the simulation framework can handle wide ranges of energy distribution accurately we compared measurements and simulation for the complete white beam spectrum of ICON as well as the Be-filtered spectrum. The simulation is capable of describing the effect of broad wavelength distributions as can be seen in Fig. 3. The reason for the increased visibility of the Be-filtered spectrum over the white beam is that the Be-filter removes neutrons with wavelengths below 4 Å. As can be seen in eq. 2 the transmission is highly wavelength dependent and smaller wavelengths are less absorbed and thus do not contribute as much to the visibility as longer wavelengths neutrons.

Besides the variation in wavelength distribution we also checked the robustness of the simulation for changes in hardware. For that a setup in the third fractional Talbot distance was used that

Optics EXPRESS

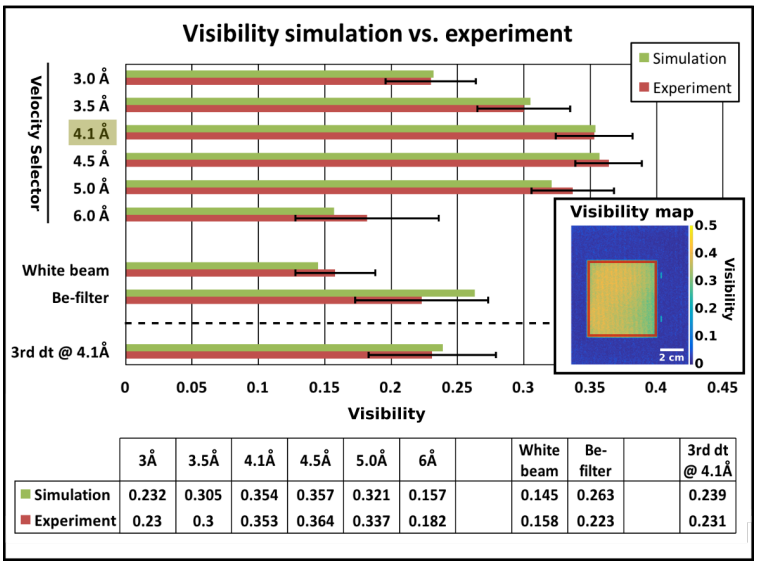

	3Å	3.5Å	4.1Å	4.5Å	5.0Å	6Å		White beam	Be-filter		3rd dt @ 4.1Å
Simulation	0.232	0.305	0.354	0.357	0.321	0.157		0.145	0.263		0.239
Experiment	0.23	0.3	0.353	0.364	0.337	0.182		0.158	0.223		0.231

Fig. 3. Comparison of experimental and simulated visibility values for varying measurement conditions. The top six values are monochromatically recorded visibilities, including the design wavelength of the setup 4.1 Å. A velocity selector is used to vary the neutron wavelength. The white beam and Be-filtered spectra are the full spectrum of the beamline and the full spectrum with a cut-off at 4 Å keeping only the larger wavelengths. The inlet shows a visibility map with the area of extracted visibility indicated as a red box. The measured as well as the simulated values can be found in the table on the bottom of the figure.

has different grating characteristics. It includes G0 and G1 gratings with different periods than for the first fractional Talbot distance. We also varied the duty cycle of G0 and measured with a duty cycle of 0.5. This impacts the coherence of the beam, which is determined by the G0 size. As can be seen in Fig. 3 the simulation framework handles the changes in beam coherence very well and is capable of describing the third fractional Talbot distance setup accurately.

All in all the simulation is capable of describing the visibility changes for both spectral and geometrical variation. Most notably the variation in setup geometry is remarkably well represented, which gives us confidence in the physically correct implementation of the real setup. The quantitative nature of the simulation model presented here is purely based on the real geometry of the gratings and the measured spectra of the beamline. It makes it possible to separate the individual contributions to reduced visibility and to quantify the individual impact on the performance.

Individual contribution to reduced visibility

Three individual contributions to reduced visibility are identified, which are spectral distribution, geometry of G1 and geometry of G2. All of those contribute to the reduced visibility differently, as illustrated in Fig. 4. The theoretical limit for the maximum possible visibility with the setup designed for ICON is 0.6, represented by the green colour. The maximum possible visibility of 0.6 is a consequence of the beam coherence that is dominated by the G0 duty cycle of 0.4. This behaviour is visible in the simulation with perfect grating geometries, as well as by calculating the maximum possible visibility using the equations in [13].

We quantify the individual contributions to a reduced visibility by following the matrix on the top right in Fig. 4. First we determine the visibility for an ideal setup, then we include the real

Optics EXPRESS

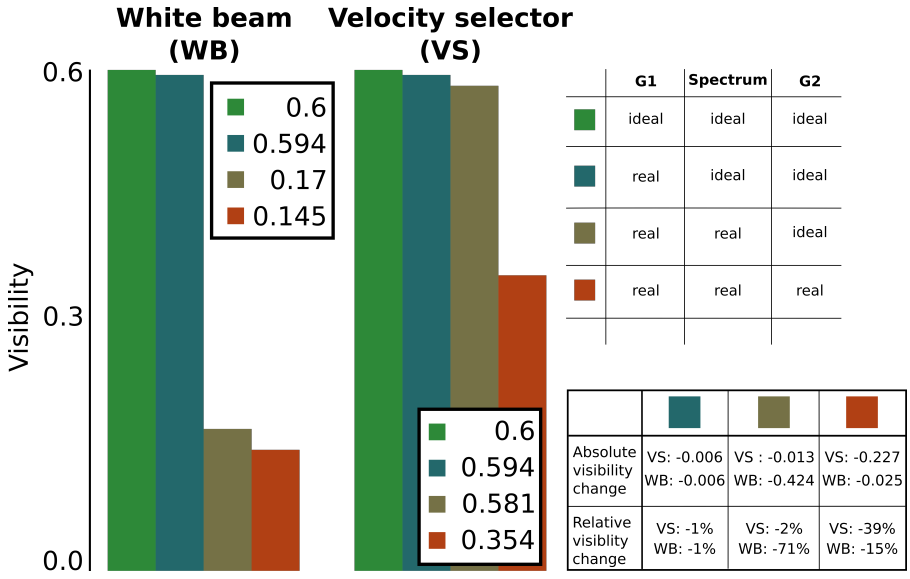

	G1	Spectrum	G2
	ideal	ideal	ideal
	real	ideal	ideal
	real	real	ideal
	real	real	real

Absolute visibility change	VS: -0.006 WB: -0.006	VS : -0.013 WB: -0.424	VS: -0.227 WB: -0.025
Relative visiblity change	VS: -1% WB: -1%	VS: -2% WB: -71%	VS: -39% WB: -15%

Fig. 4. Step wise consideration of different real effects to decreased visibility. The impact of real geometries of G1 and G2 as well as the energy resolution of the velocity selector can be judged individually by the relative decrease in visibility attributed to each feature. The bar plot visualises the different contributions for white beam measurements as well as measurements at the design wavelength of 4.1 Å, selected with a velocity selector. The table on the bottom shows the absolute and relative contributions of the individual simulation setups as indicated in the simulation scheme on the top right.

geometry of G1, then the real wavelength distribution and then the real geometry of G2. This procedure was done for a white beam (WB) simulation, as well as for the design wavelength selected with the velocity selector (VS). The individual contributions vary depending on the spectrum used.

Both simulations show the same behaviour for an ideal setup and result in a simulated visibility of 0.6. Also the inclusion of the ideal G1 geometry shows the same behaviour, as the spectrum is not considered yet. The simulated visibility drops by 1% to 0.594. Once we take the real spectral distribution into account the behaviours of WB and VS measurements vary significantly with a relative decrease of -71% for the WB simulation and -2% for the VS simulation. Thus after the consideration of the real G1 geometry and the real spectral distribution we get a simulated visibility of 0.17 for WB and 0.581 for VS. The last contributor to decreased visibility is the real geometry of G2 which introduces another 15% drop for WB and a 39% drop for VS. Thus the major contributors to a decrease in visibility is either the spectrum (WB) or the geometry of G2 (VS).

This shows, that if the performance of nGIs was to be improved there are two things to consider. If the main application of the setup is to measure with white beam, then the geometry of the gratings is sufficient as the energy distribution is the main contribution to a reduced visibility. The setup at ICON is close to the best possible performance it can reach with white beam. However if mostly images with a velocity selector are recorded, then the geometry of G2 is the major contributor to a reduced visibility and the influence of the velocity selector is relatively small. Thus grating fabrication has to be improved to increase visibility. Surprisingly the imperfection of G1 is not contributing much to the decrease of visibility, despite its strong impact on the

Optics EXPRESS

Talbot carpet, as shown in Fig. 2.

5. Conclusion

The approach presented in this work does not only hold for the nGI at ICON, but is a framework for all grating interferometer setups, including X-ray experiments as well as other neutron beamlines. We can use the simulation framework to evaluate the feasibility to do grating interferometry at different beamlines and predict the expected performance. One example is the BOA beamline at PSI [21], which has a colder spectrum than ICON. Our simulation predicts excellent performance of the nGI at BOA with a visibility of around 22 % with a white beam, compared to 14.5 % at ICON. Thermal beamlines however are putting different requirements on the gratings, as the higher neutron energy demands a greater thickness of Gd for absorption, otherwise the visibility is decreased. Our simulation predicts a visibility of merely 5.3 % if we would put the ICON nGI setup simulated here to the thermal beamline NEUTRA. This is comparable to high energy X-ray grating interferometers [17, 22]. The visibility could potentially be improved by designing dedicated grating interferometers for thermal neutron beamlines. The completely quantitative modelling approach we used in this work does not only allow the performance evaluation for different beamlines, but can also be used to design new grating interferometers at higher Talbot orders or varying phase shift. Also the performance of X-ray grating interferometers could be included. Here the identification of the contributions to the loss in visibility can be important to further increase the contrast. Finally, the generality of the modelling framework allows us to quantify performances before building actual devices, thus making it possible to dream up new designs and test them right away without depending on a real experimental setup.

Funding

Swiss National Science Foundation (SNSF) (153304)

Acknowledgments

The authors gratefully acknowledge M. Horrisberger for the sputtering of the G0 substrate and R. Brönnimann for help with the laser ablation. We would like to thank Ch. Ruegg, A. Kaestner, S. Peter, B. Betz and E. Lehmann for fruitful discussion and J. Hovind for manufacturing the mechanical parts of the setup.